Engineering Porosity-Tuned Chitosan Beads: Balancing Porosity, Kinetics, and Mechanical Integrity

Astha Upadhyay[†], Farbod Alimohammadi[†], Rouzbeh Tehrani*

Department of Civil and Environmental Engineering, Temple University, Philadelphia, PA 19122

[†]These authors contributed equally to this work and shared first authorship

**Email: r.tehrani@temple.edu*

Abstract

Chitosan, a cationic natural polysaccharide derived from the deacetylation of chitin, is known for its solubility in diluted acidic solutions, biodegradability, biocompatibility, and non-toxicity. This study introduces three innovative methods to prepare porous chitosan microsphere particles, which are crucial for enhancing their efficiency in water remediation and medical applications. The methods, solvent extraction, surfactant extraction, and substance decomposition, involve the integration and subsequent extraction or decomposition of materials during the synthesis process, eliminating the need for additional steps. We used state-of-the-art characterization techniques to analyze and evaluate the chemical and physical properties of the particles, such as Fourier-transform infrared spectroscopy (FT-IR), scanning electron microscopy (SEM), X-ray diffraction (XRD), and especially three-dimensional computed tomography (CT) scanning. The CT scans were used to visualize and measure the porosity of different particle types, ranging from 68.4% to 39.3%. This detailed study extended to evaluate the mechanical properties of the particles under compressive forces in wet and dry conditions, highlighting the influence of porosity on their mechanical integrity and compression pressure behavior. In addition, we explored the adsorptive properties of these chitosan particles, using methylene blue as a model pollutant because of its toxicity, underscoring the significance of porosity in enhancing their pollutant removal efficiency. This study opens the window for developing environmentally sustainable polymer particles and highlights the pivotal role of porosity in optimizing the material's efficacy for a wide range of applications.

Introduction

Chitosan is a natural polysaccharide; the deacetylation of chitin can obtain it.[1-3] Chitin is the most abundant natural polymer after cellulose.[3] The application of chitin is limited because it is insoluble in most solvents, while chitosan is soluble in diluted acidic solutions.[3] Chitosan is

extensively used as a scaffold or hydrogel for various applications such as tissue engineering and drug deliveries.[3-4] Chitosan is a biodegradable, biocompatible, nontoxic, and low-cost polymer, making it a great candidate for industrial-scale applications.[3] Chitosan has been widely used to remove heavy metals, microorganisms, organic and inorganic compounds from wastewater [3, 5-8] and can be functionalized or serve as templates for embedding inorganic materi`als.[1, 3, 5-7, 9-11]

The porosity of the chitosan can play a crucial role in the efficiency of polymer for water remediation and medical applications.[1, 4-5, 8, 12-14] Introducing porous morphology to the particles provides additional active sites and surface area for removing the pollutants or loading of drugs.[1, 4-5, 8-9] Various methods are introduced to prepare porous chitosan. They can be classified into four different strategies including freeze-drying[1, 15-16], sol-gel[1, 17-18], phase inversion[1, 19] and using a porogen agent.[1, 20] The conventional method is the freeze-drying method (also known as lyophilization), it involves the freezing of the solvent at low temperature and then removal of the solvent by sublimation under a vacuum which leads to the formation of porous structures.[1, 15] However, the freeze-drying process is time-consuming and expensive which limit its application for industrial scale. The sol-gel strategy is similar to the freeze-drying method, while the sample is not frozen and dried under supercritical conditions. [1, 17-18] Phase inversion is another common method to prepare porous polymer.[1, 19] There is a solvent exchange with non-solvent, and precipitation occurs to form a porous structure.[1, 19] Another method is based on the addition of a porogen agent, which can be extracted by leaching.[1, 20-21]

Controlling the size and porosity of the polymeric particles is pivotal in determining their physical and chemical characteristics..[4, 22] Typically, chitosan microsphere particles are synthesized by dissolving chitosan polymer in dilute acetic acid, followed by the formation of a hydrogel. [23-24] Subsequently, elevating the pH of the polymer solution deprotonates the chitosan, diminishing the solubility of the polymer chains, and results in the formation of microsphere particles through van der Waals forces, hydrogen bonding, and hydrophobic interactions. .[23-24] We present three distinct approaches for synthesizing porous chitosan microsphere particles, each involving the incorporation of a material into the polymer solution, followed by its subsequent extraction or decomposition during synthesis. These approaches are classified as solvent extraction, surfactant extraction, and substance decomposition. The solvent extraction technique employs an oil-in-

water (O/W) emulsification process, wherein the organic phase, specifically 2-Methylpentane, is integrated into the chitosan solution (aqueous phase). Subsequently, the organic phase is removed during the synthesis procedure. In an alternative approach, a polysorbate surfactant is introduced to the polymer solution and subsequently eliminated from the polymer microsphere particles during synthesis. The final method involves the addition of azodicarbonamide to the chitosan solution, followed by its decomposition throughout the synthesis process. Notably, these processes do not require any additional steps during synthesis.

Our research is dedicated to the precise tuning and control of the pore structure in chitosan particles to optimize their application in water treatment. The structural properties of chitosan microsphere particles are studied using Fourier-transform infrared spectroscopy (FT-IR), scanning electron microscopy (SEM), and X-ray diffraction (XRD). The three-dimensional (3D) CT scanning was applied to study and compare the porosity of different particles. The mechanical properties of the single particles were studied to investigate the mechanical stability of porous particles under compression in wet and dry conditions. Methylene blue, a water-soluble dye, is widely used as a model contaminant in water treatment research. Its ease of detection and resemblance to a wide range of organic pollutants render it an excellent standard for assessing water purification methods, notably adsorption and filtration techniques. [25-26] Thus, in this study, methylene blue was used as a model contaminant to assess its removal efficiency by chitosan microsphere particles varying in porosity. In addition to evaluating mechanical and physical properties, our aim was to achieve an optimal balance among porosity, kinetics, and mechanical strength, targeting a synergistic enhancement of adsorption performance and structural integrity.

Methods and material

Materials

Low molecular weight chitosan (75–85% deacetylation, and a molecular weight range: 50,000-190,000 Da), glutaraldehyde, azocarboxamide, fluorescein isothiocyanate isomer I (90%), glacial acetic acid, sodium hydroxide and polysorbate 20 (Tween 20) were purchased from the Sigma-Aldrich company. All chemicals were used as received without further purification.

Synthesis

Two grams of low molecular weight chitosan polymer was dissolved in 80 ml glacial acetic acid solution (2%) at 70°C. The obtained chitosan solution was added dropwise into a NaOH aqueous solution (1M). The beads were aged overnight and then rinsed with DI water to obtain a neutral pH. Then, the beads were added to glutaraldehyde solution (5%) to cross-link the microsphere particle overnight. The cross-linked microsphere particles were washed with DI water and were dried at room temperature.

The porous microsphere particle was synthesized using the same procedure but with three different additives to the chitosan solution. The first method is based on the addition of the organic phase/surfactant to the polymer solution; 10 ml of 2-methylpentane (as organic phase) and 24 ml of tween 20 (as surfactant) were mixed and then added to the polymer solution, the sample made from this method is named PCP-M. The second method is based on adding a porogen agent (4 g of azocarboxamide) to the chitosan solution. Beads made by using azocarboxamide are named PCP-A. In the last method, 35 ml of tween 20 (a porogen agent) was added to the polymer solution, the PCP-T sample. In summary, "PCP" denotes porous chitosan particles, "M" represents 2-methylpentane, "A" signifies azodicarbonamide, and "T" refers to Tween 20.

Characterization

Synthesized porous chitosan microspheres and non-porous chitosan microspheres were characterized by X-ray diffraction (XRD) using a Bruker D8 X-ray diffractometer with Cu Kα radiation (λ = 0.15406 nm), Fourier transform infrared spectroscopy (FTIR) using a PerkinElmer Spectrum 100 FT-IR spectrometer, scanning electron microscopy (SEM) using FEI Quanta 450 FEG, and fluorescent microscopy (FM).

A Bruker D8 X-ray diffractometer with Cu Kα radiation (λ = 0.15406 nm) obtained X-ray powder diffraction patterns of tuned chitosan microspheres and non-porous chitosan microspheres. DIFFRAC.EVA software was used to determine the crystallite size of the samples. Samples were scanned from 5–80° (2θ value), 0.02° step, and 0.3 s per step.

FTIR-attenuated total reflection (ATR) analysis was conducted using a PerkinElmer Spectrum 100 FT-IR spectrometer. The spectra were obtained from 400 to 4000 cm^{-1}, with 2 cm^{-1} resolution and

4 accumulated scans per sample (n=5). The spectral peaks were identified using a second derivative plot, and assignments were done using available literature. The data were used to identify the functional group present in the chitosan microspheres synthesized using different processes.

SEM imaging was done by FEI Quanta 450 FEG scanning electron microscope (SEM) equipped with energy-dispersive X-ray spectroscopy (SEM-EDS). The instrument was used at 5 kV, and the samples were mounted on carbon tape. Fluorescent imaging was done using an Olympus Fluorescent microscope. The porous and non-porous chitosan microspheres were individually placed in the microscope with one mg/L fluorescein isothiocyanate isomer I (90%) dye. The microscope was at 10x magnification, and different z-stack images were captured.

A high-resolution X-ray computed tomography instrument, The Rigaku Nano3DX, was used to scan the particles' 3D structure. A copper target with fields of view of 3.6 x 2.8 mm was used.

Nitrogen isotherms were performed at 77°K using an ASAP2460 instrument. The specific surface area was calculated using Brunauer, Emmett, and Teller (BET), Langmuir, and t-plot external. The total pore volumes were calculated from the amount of nitrogen adsorbed at P/P0, 0.9947, 0.9956, 0.9944, and 0.9947 for the control, PCP-M, PCP-T, and PCP-A, respectively.

Adsorption studies

Methylene blue removal was monitored via a UV-Vis spectrophotometer. The UV-Vis spectra for both porous and non-porous chitosan microspheres were acquired at 664 nm using a DR 5000 UV-Vis spectrophotometer (number of replicates, n=3). Preliminary experiments were carried out at pH levels of 2, 4, and 6 to identify the optimal pH for effective adsorption, with pH 6 being chosen for subsequent adsorption studies. A calibration curve was plotted using 0.1, 0.2, 0.5,1.0, and 2.0 mg/L concentrations of methylene blue (MB) solution (included in supplementary information Figure S1). Freundlich isotherm was obtained by plotting 10, 25, 50, 100, 150, and 200 mg chitosan microspheres in 5mL of 2 ppm MB solution. The absorbance was recorded at 15, 30, 60, 90, 150, 210, 1440, and 2880 minutes. Fruendlich and Langmuir isotherms are extensively discussed and presented in numerous studies. [25-26]

Adsorption kinetics

The kinetic model describing the adsorption process for non-porous, PCP-M, PCP-T, and PCP-A was analyzed using adsorption capacity versus time data. The equations below were utilized to assess the kinetics and mechanism of adsorption:

$$\ln(q_e - q_t) = \ln q_e - k_1 t \quad \text{(pseudo-first-order kinetic model)} \quad [1]$$

$$\frac{t}{q_t} = \frac{1}{k_2 q_e^2} + \frac{t}{q_e} \quad \text{(pseudo-second-order kinetics model)} \quad [2]$$

where q_t (mmol/g) and q_e (mmol/g) denote the uptake amount at time t (min) and at equilibrium time t (min); k_1 (1/min) and k_2 (g/mmol/min) represent the rate constant of these models, respectively. [25-26]

Mechanical properties

The synthesized non-porous and porous microspheres were tested for their mechanical properties using Caldaro position sensors (Caldaro sadae, Japan) and Deben Microtest tensile stage. Deben Microtest software (V6.1.51) was used to process the data, and deformation resistance was calculated from the nominal stress and strain curve. The ramping velocity during this work was 0.2 mm/min. Furthermore, the microspheres were soaked in water for 1 hour to determine the effect of dampness on the mechanical strength. Nominal stress was calculated by dividing the force by the cross-sectional area of microspheres and a nominal strain by dividing displacement by the diameter of the SP before compression. The slope in the linear region of the stress-strain curve is used to evaluate the deformation resistance of elastic material. Similarly, the nominal stress and strain at the first inflexion point, where the first fracture occurs, was defined as the yield strength of the material. The size of the porous particles was around 2.0-2.4mm, and the diameter of the control particle was 1.5-1.8mm. The analysis was repeated at least two times. The force−distance curves resulting in extremely high or low stiffness were excluded. When the tip was in contact with the substrate instead of the top of the microsphere, inaccurate high stiffness was recorded. Unacceptable low stiffness values were observed when the tip contacted the side of the microspheres, and lateral motion occurred.

RESULTS

Imaging

SEM and Fluorescent imaging of non-porous microspheres and synthesized PCP-M, PCP-A, and PCP-T are shown in **Figure 1**. SEM images of the non-porous microsphere proved the absence of pores, and the FM images did not show any fluorescence due to the lack of pores. PCP-M, PCP-A, and PCP-T microspheres showed porosity in both SEM and PM images. Numerous factors, such as the quantity and variety of porogen, monomer composition, drying conditions, and crosslinking agents, can influence the pore structure.[27] The pore size of PCP-A was the largest, followed by PCP-M, while PCP-T exhibited the smallest pore size, leading to a high-density, finely porous network. Z-stack imaging of PCP-M and PCP-A microspheres revealed highly branched pores and extensive tunnel-like structures, respectively. Corresponding SEM images confirmed these structures, highlighting the distinct impacts of each porogen on the microspheres' morphology.

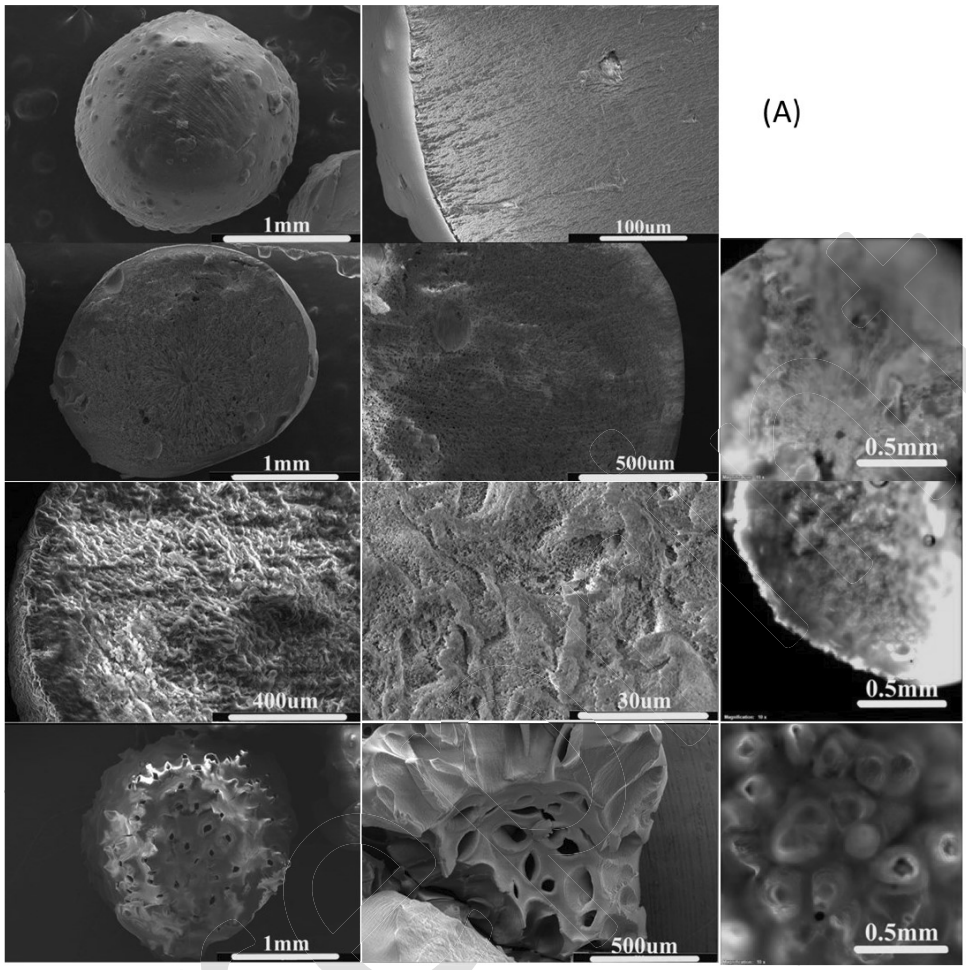

Figure 1. (A) SEM images of non-porous microspheres. SEM and FM images of (B) PCP-M, (C) PCP-T, and (D) PCP-A microspheres

BET

A nitrogen adsorption-desorption experiment evaluated the particles' surface area, pore size, and pore diameter (**Figure 2**). International Union of Pure and Applied Chemistry (IUPAC) classified nitrogen adsorption-desorption isotherms; our samples show the type IV behavior with H3 hysteresis loops. Type IV isotherm appears when there is an interaction between gas molecules and adsorbent mesopore surface, leading to capillary condensation. Type IV isotherm corresponds to micro and mesopores in the substance.

The BET, Langmuir, and t-Plot external surface area of samples arise after introducing porosity to the particles (**Table 1**). The surface area of the PCP-T and PCP-M are significantly higher than the control. Although the surface area of PCP-A is more elevated than the control, it is notably lower than PCP-M and PCP-T. SEM results confirmed that the microporous structure is more dominant in the PCP-A sample. The results suggest PCP-T shows a higher surface area and smaller pores than PCP-M.

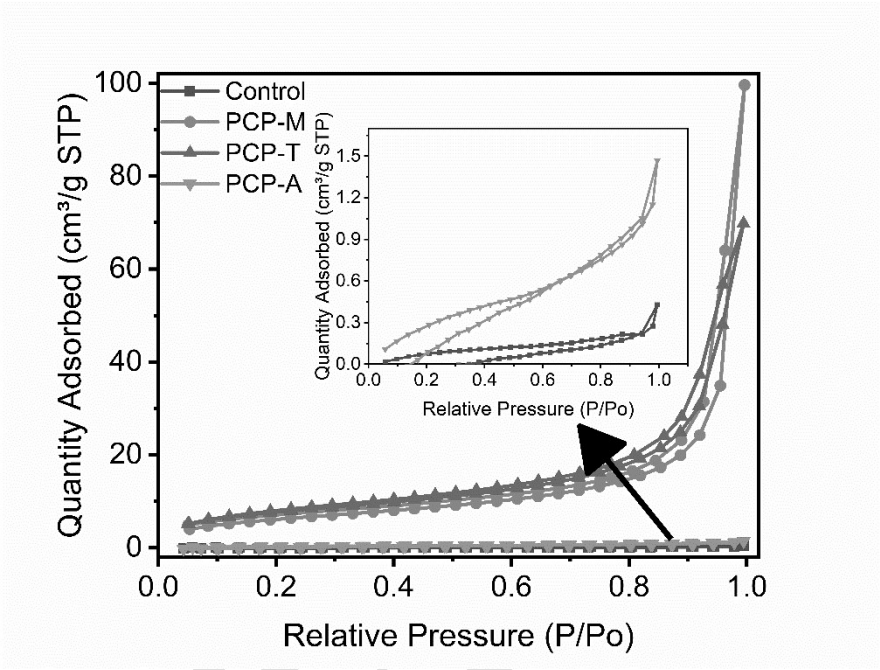

Figure 2. Nitrogen adsorption and desorption curve of the chitosan particles.

Table 1 shows the surface area, pore size, and pore diameter of chitosan particles. The total pore volume and pore diameters were calculated from the N2 adsorption isotherms.

Samples	**BET Surface Area (m^2/g)**	**Langmuir Surface Area (m^2/g)**	**t-Plot external surface area (m^2/g)**	**Total pore volume of pores (cm^3/g)**	**Adsorption average pore diameter (nm)**	**BJH Adsorption average pore diameter (nm)**	**D-H Adsorption average pore diameter (nm)**
Control	0.32	1.24	0.47	6.64×10^{-4}	8.28	13.06	6.92
PCP-M	21.19	111.53	23.90	0.15	28.81	30.79	9.47
PCP-T	25.76	126.71	27.59	0.11	16.77	19.66	16.07
PCP-A	1.23	6.84	1.72	2.272×10^{-3}	7.37	10.03	6.46

X-ray CT images

Figure 3 presents a series of X-ray CT images illustrating the cross-sections of chitosan particles. The images are categorized into three sets, labeled as PCP-M, PCP-T, and PCP-A, each comprising of three images: a 3D pore image at the top, a 3D particle image in the middle, and a 2D single slice image at the bottom. The 3D pore images vividly display the porous architecture of the particles, allowing for a clear visualization of the interconnected porosity within the chitosan particles. The 3D particle images provide a comprehensive view of the particle morphology, offering insights into their structural integrity and overall form. Meanwhile, the 2D single-slice images provide a detailed view of the internal structure of the particles, enabling a closer examination of the pore distribution and wall thickness.

Quantitative image analysis revealed variances in the porosity of the particles, with the PCP-M particles exhibiting a porosity of 68.4%, followed by the PCP-A particles at 65.0%, and the PCP-T particles showing the lowest porosity at 39.3%. This quantitative data, in conjunction with the visual insights from the images, allows for an understanding of the structural characteristics and porosity of the chitosan particles. PCP-M particles are highly porous with a moderate surface area, making them suitable for applications requiring substantial internal spaces, such as drug encapsulation or delivery. On the other hand, PCP-A shows a high porosity but significantly lower surface area; these particles might be limited in applications requiring substantial surface interactions but could still be useful in applications necessitating internal carrying capacities, such as controlled release of substances.

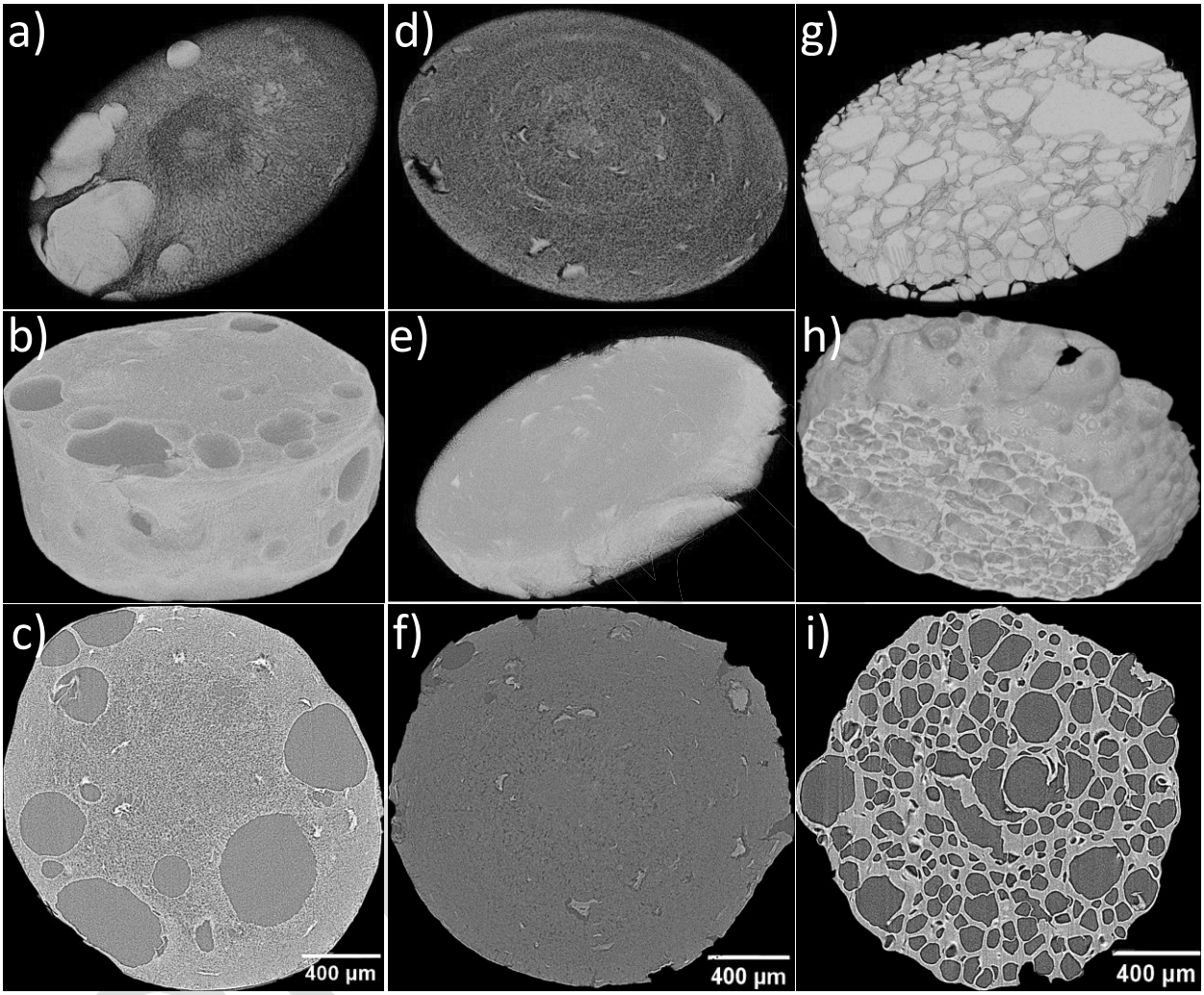

Figure 3. X-ray CT images from the cross-section of the chitosan particles, a, b, and c) PCP-M, d, e and f) PCP-T, g, h, and i) PCP-A, the 3D images of the pores at the top, the 3D images of the particles at the middle, and 2D single slice images at the bottom. The image analysis showed 68.4%, 39.3%, and 65.0% porosity for the PCP-M, PCP-T, and PCP-A, respectively.

XRD

XRD patterns of the powdered, synthesized, non-porous, and porous chitosan microspheres were obtained to determine the crystalline structure (Figure 4). From the pattern, the two characteristic peaks at 10° and 20° of the extracted chitosan with a crystalline structure. Powdered pristine chitosan had an intense peak at 20° with a sharp peak corresponding to the chitosan phase. Similar peaks of the chitosan phase were observed in synthesized chitosan. The peak broadening observed in the porous chitosan microsphere at 20° indicates the polymorphic structure and deviation from perfect crystallinity. Among the synthesized porous microspheres, PCP-M showed the sharpest peak at 20°. The crystallinity and crystallite size of the chitosan particles are shown in Figure 4b; crystallinity of the particles decreases by introducing porosity to the structure. The crystallite size of the particles was calculated using the peak at 20°and they are in the range of 20-40Å.

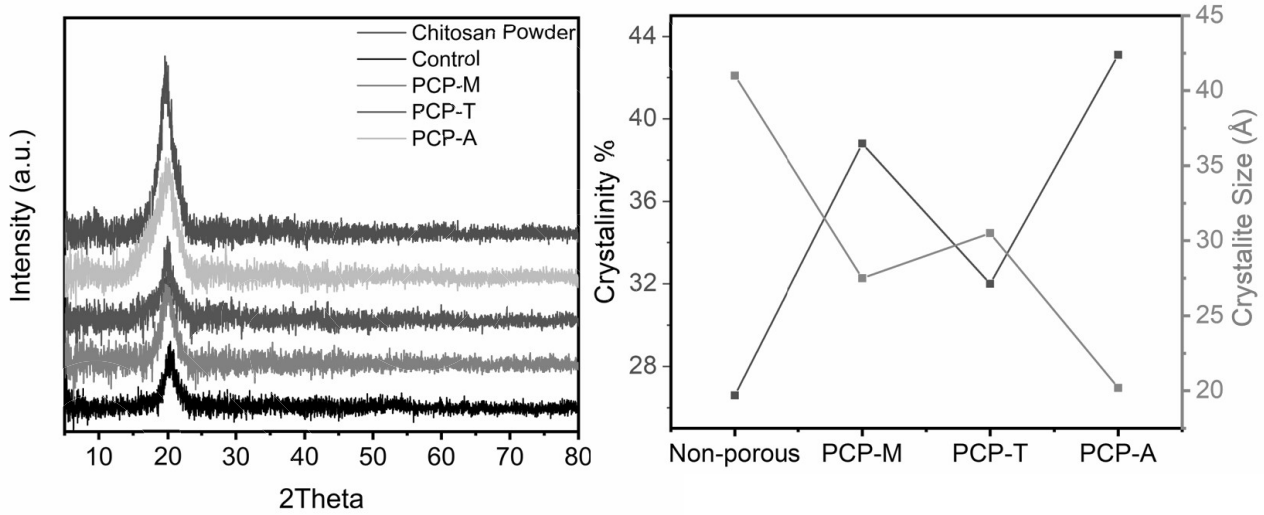

Figure 4. a) XRD diffractogram of non-porous chitosan microspheres, fine-tuned chitosan microspheres, namely PCP-M, PCP-T, and PCP-A, and powdered chitosan, b) crystallinity and crystallite of the chitosan particles.

FTIR and TGA

In **Figure 5**, we can observe the infrared spectrum of chitosan. A strong band in the region 3291–3361 cm^{-1} corresponds to N-H and O-H stretching, as well as the intramolecular hydrogen bonds. The absorption bands at around 2921 and 2877 cm^{-1} can be attributed to C-H symmetric and asymmetric stretching, respectively. These bands are characteristics typical of polysaccharides and are found in other polysaccharide spectra, such as xylan, glucans, and carrageenan. The powder chitosan and PCP-M peak around 2921 and 2877 cm^{-1} had lower intensity, indicating similar stretching, whereas PCP-A and PCP-T had higher intensity bands. The presence of residual-acetyl groups was confirmed by the bands at around 1645 cm^{-1} (C=O stretching of amide I) and 1325 cm^{-1} (C-N stretching of amide III), respectively. The band corresponding to the N-H bending of amide II was missing at 1550 cm^{-1} in powder chitosan, indicating possible overlap with other bands, but a small band was observed in the synthesized porous samples. The 1423 and 1375 cm-1 bands confirm the CH_2 bending and CH_3 symmetrical deformations, respectively. The absorption bands at 1153 cm^{-1} and 1066 and 1028 cm^{-1} can be attributed to the asymmetric stretching of the C-O-C bridge and C-O stretching, respectively. All bands are found in the spectra of samples of chitosan reported previously.[28]

The TGA curves of chitosan particles exhibit weight loss in three stages, as shown in **Figure 6**. The first stage appeared in the 40-100° C range, which can be attributed to the water loss. The water weight loss is around 0.9% for the control sample, while it is significantly higher for the porous particles, around 6-11%. The second degradation is around 280°C. A change of the thermogram curve at 430°C suggests a slower third process. Another process was observed in the derivative curve between 550-650°C. The correspondent derivative curve reached zero between 650-800°C with no evident distinct events. The FTIR analysis conducted on the samples previously demonstrated the presence of certain peaks corresponding to certain functional groups.

Previous research has reported that evolved gas mainly composed of H_2O, NH_3, CO, CO_2, CH_3COOH, and CH_4 is released during the degradation of chitosan.[27] A main process involving the release of H_2O, NH_3, CO, CO_2, and CH_3COOH is assigned to the pyrolytic degradation of chitosan and assessed in the literature in the temperature range 250-450°C.[27] In the temperature range of 225-450°C, a weight loss of ~ 55 wt.% was observed, possibly corresponding to this gaseous

release. At lower temperatures, the release of NH_3 release is initiated, which reaches its peak at 325°C, suggesting a low activation energy for NH_3 formation. A second process characterized by the release of CH_4 possibly happened in the range 550-650°C, corresponding to a loss of~ 31 wt. %. The highest rate of CH_4 generation is observed at around 590°C in control chitosan, as observed in the previous studies.[1] The synthesized microspheres have a deviation in the peak between 550-650 °C, with the maximum generation of CH_4 observed around 550, 580, and 650 °C for PCP-M, PCP-T, and PCP-A, respectively. A modification of the material is suspected after the complete reduction of the structure, causing methane production and the consequent formation of a graphite-like structure via a dehydrogenation mechanism, as suggested in the literature.[29-30] Monitoring the evolution of species in temperature/time scale is imperative to identify a complex degradation pattern.

302

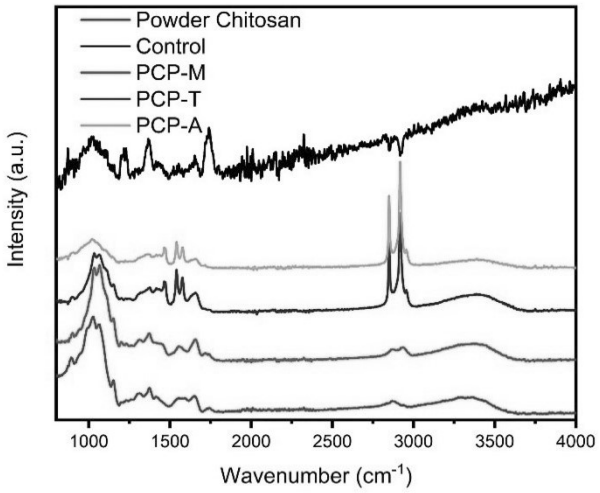

303

304 **Figure 5.** FTIR spectra of the porous chitosan microspheres and powdered chitosan

305

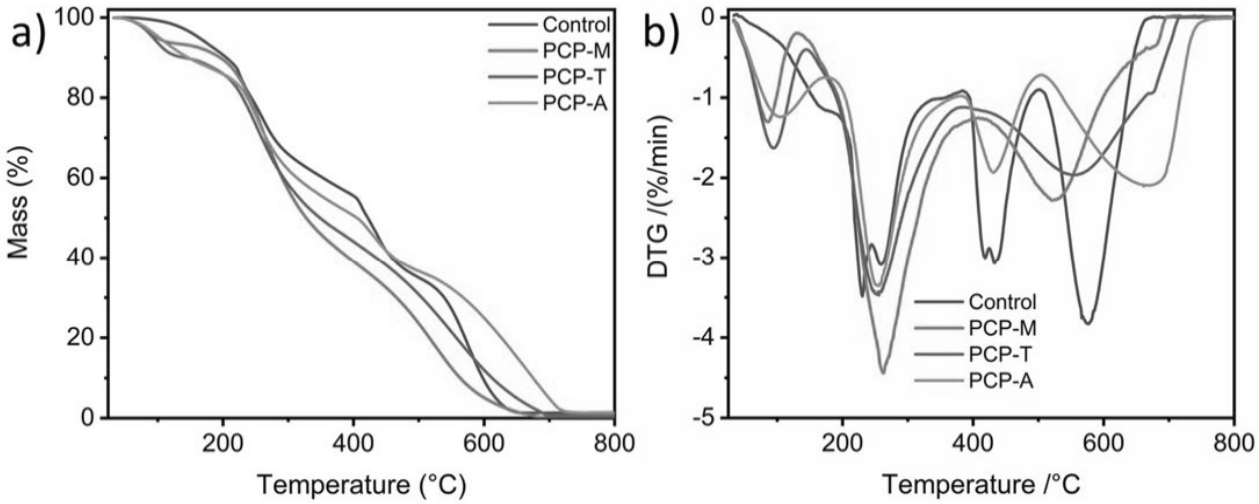

306

307

308 **Figure 6.** a) thermogravimetric analysis of the chitosan particles, b) derivative

309 thermogravimetry of chitosan particles.

310

311

Adsorption isotherm and adsorption kinetics

As shown in **Figure 7**, the methylene blue removal in samples was significant in synthesized porous microspheres compared to the non-porous microsphere. The uptake in porous microspheres increased with time before reaching equilibrium. The removal exceeded 90% at the equilibrium value after 1440 minutes, rapidly increasing after the initial 120 min, indicating fast adsorption. The non-porous microspheres showed the lowest equilibrium removal, possibly due to decreased accessibility for mass diffusion and lack of a porous network. PCP-M showed the highest q_e and k_2, consistent with its high uptake and removal rate.

The isotherms were derived using the Freundlich and Langmuir models. The isotherm plots of the Freundlich and Langmuir models are shown in **Figure 7**. The Freundlich model fitted the data better, with higher correlation coefficients, indicating that the dye removal followed reversible multilayer adsorption by the heterogeneous surface of the microsphere. Furthermore, the Freundlich equation predicts that the dye concentrations on the adsorbent will increase with an increase in the dye concentration in the liquid phase.[31]

An investigation was conducted to examine the kinetics governing the adsorption process of the microspheres. The pseudo-first-order and the pseudo-second-order kinetic models were applied to analyze the adsorption kinetics. The pseudo-second-order kinetic model was more suitable for the overall adsorption process (after 2880 min), with higher correlation coefficients than those of the pseudo-first-order kinetic model, indicating the primary mechanism of chemical adsorption. The fitted curves by this model are shown in **Figure 7**. The PCP-M microspheres showed a higher equilibrium removal q_e and a lower rate constant k, possibly due to improved accessibility for mass diffusion.

Table 2. Adsorption isotherm of synthesized porous and non-porous chitosan microspheres

Sample	**Freundlich Isotherm**		
	k	n	R^2
Non-Porous	4.436×10^{-8}	0.095	0.98
PCP-M	1.361×10^{-04}	2.41	0.99
PCP-T	1.039	13.66	0.93
PCP-A	3.273×10^{-05}	2.60	0.87

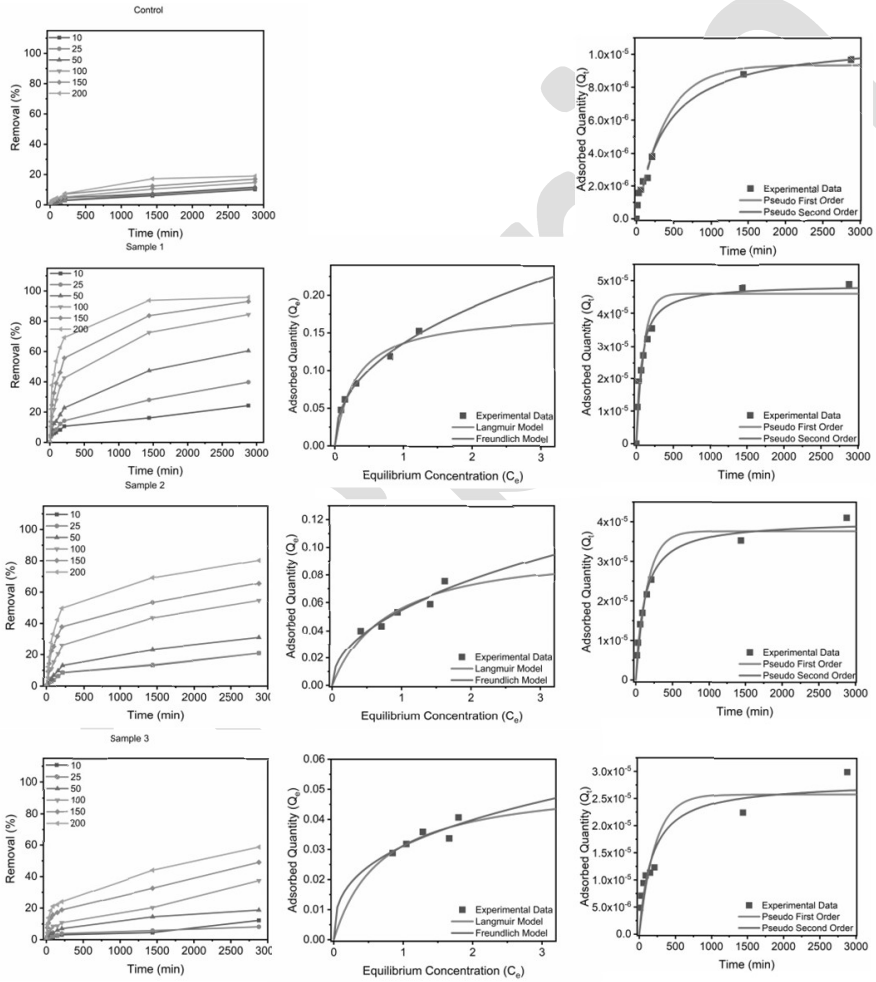

Figure 7. Concentration of MB removed from the solution by (A) non-porous, (B) PCP-M, (E) PCP-A (E), and (G) PCP-T., the **left column** depicts the removal rate (%) over time, the **middle column** depicts Langmuir and Freundlich isotherms, and the **right column** depicts pseudo-first and pseudo-second-order kinetics.

Mechanical Analysis

The mechanical properties of the microspheres were obtained by analyzing the force−distance curves centered on the particle. **Figure 8** shows the setup of the microspheres in the MicroTesting unit. Finally, four curves for the synthesized porous and non-porous microspheres of each size were used to plot stress and strain.

During the compression, the shape of the particles changes continuously. Therefore, we use nominal stress and strain instead of stress and strain. The nominal stress (calculated by the applied force divided by the cross-sectional, as a function of nominal strain (the displacement divided by the diameter of particles) was measured to assess the elastic properties of the chitosan microspheres.

Young's modulus is determined based on uniaxial tension or compression. To measure Young's modulus of a particle, we need to determine the effective modulus of the particle using the equation below:

$$(1)\ F = \frac{2}{3} E^* \sqrt{r \times \delta^{\frac{3}{2}}}$$

F, d, and δ are applied force, particle diameter, and total displacement.[32-34] Young's modulus can be calculated from the effective modulus[32-34]:

$$(2)\ E^* = {}^{E}/_{1-\nu^2}$$

ν is the position ratio of the particles. The Poisson ratio of our particles is unknown. Therefore, we determined the slope of the nominal stress and strain as deformation resistance. Deformation resistance is equivalent to the Young Modulus and can be considered an inherent property of the materials.

Figure 9 presents the stress vs. strain plot used to determine the synthesized material's deformation resistance (DR). The material properties, morphology, and roughness of the chitosan microspheres influence the deformation resistance determined from the slope of the stress versus strain plot. **Table 3** summarizes the deformation resistance and yield strength of the microspheres, and the linear part of the nominal stress and strain slope was used to determine the deformation resistance. The non-porous chitosan microspheres had the highest deformation resistance (235.43±11.34 MPa), indicating very low elasticity. PCP-M demonstrated

the highest elasticity with DR of 7.93±0.72 MPa, followed by PCP-T (9.95±0.16 MPa). PCP-A had the lowest elasticity and highest YM of 40.92±23.79 MPa among the porous chitosan microspheres. After soaking the microsphere in water for 24 hours, the elasticity of the particles changed significantly. The deformation resistance of PCP-M (0.73±0.04) was the lowest, followed by PCP-T (2.63±0.16 MPa) and PCP-A (15.66±5.05 MPa). The elasticity of PCP-M is the lowest number in wet and dry condition, which confirms the particles are softer after introducing the porosity to the structure. Interestingly, the deformation resistance of the non-porous microsphere did not change drastically from non-soaked particles (304.06±36.31 MPa).

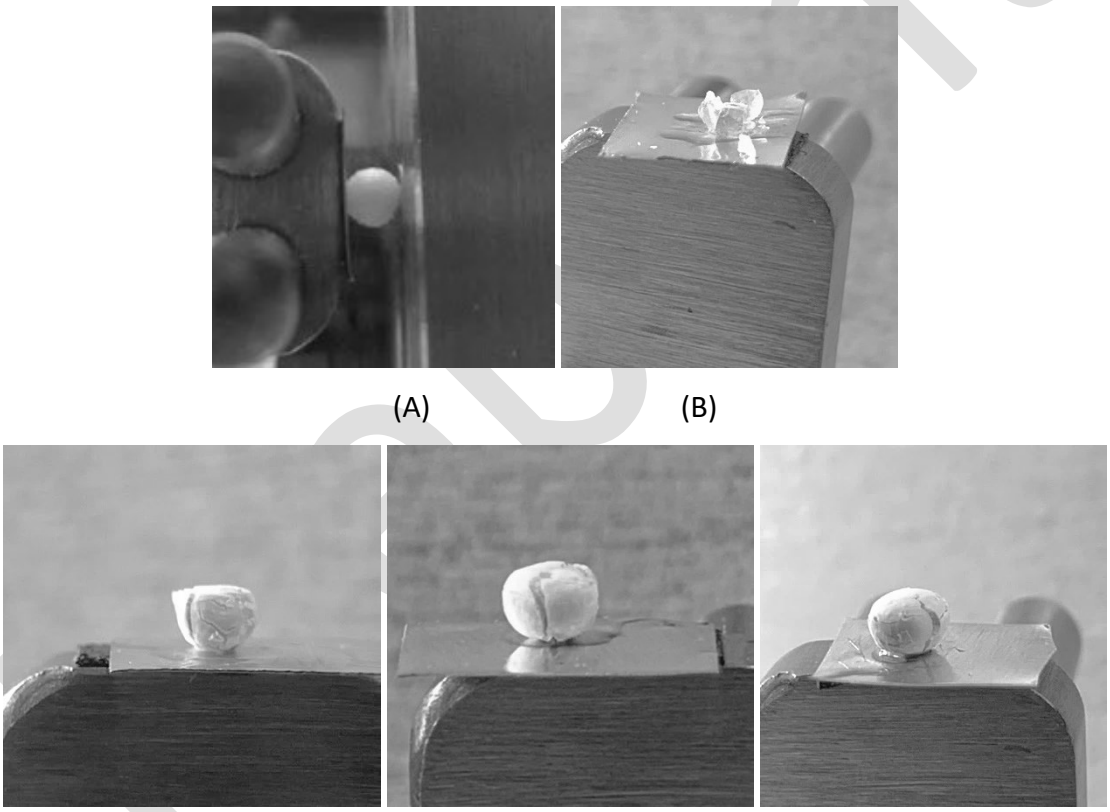

(A) (B)

(C) (D) (E)

Figure 8. (A) In-situ microtesting experimental setup. Photos taken after material failure (B) non-porous microsphere, (C) PCP-M, (D) PCP-A, and (E) PCP-T microspheres

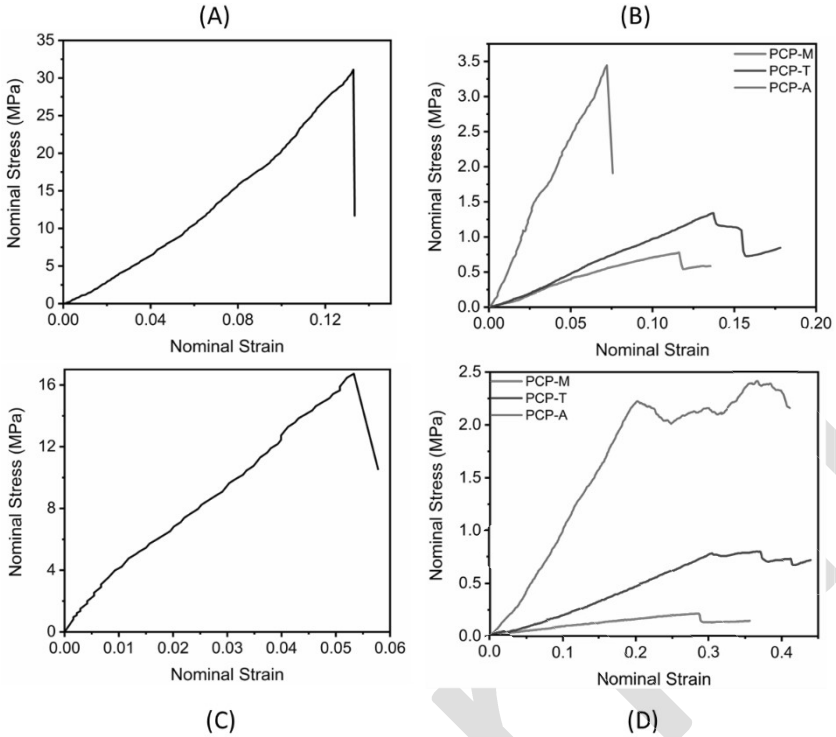

Figure 9. Nominal Stress and strain graph from the in-situ microtesting of the (A) non-porous, (B) PCP-M, PCP-A, and PCP-T microsphere, (C) Soaked non-porous, and (D) soaked PCP-M, PCP-A, and PCP-T microsphere

Table 3. Comparative summary of deformation resistance and compressive strength of the microsphere before and after 24 hours of soaking in water

Microsphere	Deformation resistance (MPa)		Compressive strength (MPa)	
	Non-soaked	Soaked	Non-soaked	Soaked
Non-porous	235.43±11.34	304.06±36.31	31.55±0.61	19.94±4.54
PCP-M	7.93±0.72	0.73±0.04	0.76±0.03	0.19±0.02
PCP-T	9.95±0.16	2.63±0.16	1.29±0.07	0.78±0.12
PCP-A	40.92±23.79	15.66±5.05	3.52±0.11	2.26±0.40

Discussion and Conclusion

We introduce a set of synthesis methods aimed to confer elasticity upon chitosan polymeric beads with structural integrity through the creation of tuned hollow-sphere microstructures. Chitosan beads were rendered porous using surfactant and porogen additives via three distinct methods. Initially, the solvent extraction method utilizing oil-in-water (O/W) emulsification was applied. Subsequently, a polysorbate surfactant was incorporated into the chitosan solution and later removed during synthesis and purification. Finally, azodicarbonamide was added to the chitosan solution, decomposing during the process. These techniques enabled the synthesis of porosity-tuned microspheres without requiring additional synthesis steps, targeting a significant reduction in cost.

FTIR and XRD analyses confirmed the chitosan phase presence and identified characteristic peaks corresponding to the chitosan structure. Comparative evaluation with pristine chitosan revealed that the porous microspheres preserved the functional and structural integrity of chitosan throughout the synthesis process. SEM and fluorescent imaging elucidated the porous network within the synthesized microspheres, contrasting with the absence of such a network in non-porous chitosan. Significant variations in pore sizes among the PCP-A, PCP-M, and PCP-T samples were observed, influencing the properties investigated in this study. X-ray CT imaging offers an in-depth analysis of the structural characteristics and porosity of chitosan particles. CT imaging, supplemented with visual assessments (SEM and fluorescent imaging), helps determine the suitability of each particle type for specific applications. This is particularly relevant given the diverse uses of chitosan beads, which span from water treatment to drug delivery.

Porous structures offer benefits over bulk counterparts, yet it's crucial for these porous beads to maintain their structural integrity under both dry and wet conditions to leverage these advantages fully. Consistent with our expectations, the introduction of porosity significantly reduces the compressive strength of the beads. Nonporous chitosan exhibited the highest compressive strength, attributable to its dense pack morphology, but did not achieve contaminant removal. When synthesizing chitosan beads, or more broadly any biopolymeric beads for water treatment, it is crucial to optimize the balance between structural integrity and the rates and capacities of contaminant removal. It is important to remember that polymers

exhibit different behaviors under compressive stress depending on whether they are in a dry or wet state. Our recommendations for future research extend beyond analyzing the behavior of beads in their wet state, as demonstrated in this study, to also assessing the shelf life of biopolymeric beads. This evaluation is crucial to ascertain whether their structural integrity alters over time.

References

1. Grzybek, P.; Jakubski, L.; Dudek, G., Neat Chitosan Porous Materials: A Review of Preparation, Structure Characterization and Application. *Int J Mol Sci* **2022,** *23* (17).
2. Shashi Kiran Misra; Pathak, K., *Microscale and nanoscale chitosan-based particles for biomedical use*. 2022.
3. Muxika, A.; Etxabide, A.; Uranga, J.; Guerrero, P.; de la Caba, K., Chitosan as a bioactive polymer: Processing, properties and applications. *Int J Biol Macromol* **2017,** *105* (Pt 2), 1358-1368.
4. Mi, F. L.; Shyu, S. S.; Chen, C. T.; Schoung, J. Y., Porous chitosan microsphere for controlling the antigen release of Newcastle disease vaccine: preparation of antigen-adsorbed microsphere and in vitro release. *Biomaterials* **1999,** *20* (17), 1603-12.
5. Wang, K.; Ma, H.; Pu, S.; Yan, C.; Wang, M.; Yu, J.; Wang, X.; Chu, W.; Zinchenko, A., Hybrid porous magnetic bentonite-chitosan beads for selective removal of radioactive cesium in water. *J Hazard Mater* **2019,** *362*, 160-169.
6. Gomaa, H.; Abd El-Monaem, E. M.; Eltaweil, A. S.; Omer, A. M., Efficient removal of noxious methylene blue and crystal violet dyes at neutral conditions by reusable montmorillonite/NiFe(2)O(4)@amine-functionalized chitosan composite. *Sci Rep* **2022,** *12* (1), 15499.
7. Vázquez, M. O.; Ramírez-Arreola, D. E.; Bernache, J.; Gómez, C.; Robledo-Ortiz, J. R.; Rodrigue, D.; González-Núñez, R., Using Chitosan as a Nucleation Agent in Thermoplastic Foams for Heavy Metal Adsorption. *Macromolecular Symposia* **2009,** *283-284* (1), 152-158.
8. Rorrer, G. L.; Hsien, T. Y.; Way, J. D., Synthesis of porous-magnetic chitosan beads for removal of cadmium ions from wastewater. *Industrial & Engineering Chemistry Research* **2002,** *32* (9), 2170-2178.
9. Zhao, H.; Xu, J.; Lan, W.; Wang, T.; Luo, G., Microfluidic production of porous chitosan/silica hybrid microspheres and its Cu(II) adsorption performance. *Chemical Engineering Journal* **2013,** *229*, 82-89.
10. Tu, N.; Shou, J.; Dong, H.; Huang, J.; Li, Y., Improved Catalytic Performance of Lipase Supported on Clay/Chitosan Composite Beads. *Catalysts* **2017,** *7* (10).
11. Wang, M.; Ma, Y.; Sun, Y.; Hong, S. Y.; Lee, S. K.; Yoon, B.; Chen, L.; Ci, L.; Nam, J. D.; Chen, X.; Suhr, J., Hierarchical Porous Chitosan Sponges as Robust and Recyclable Adsorbents for Anionic Dye Adsorption. *Sci Rep* **2017,** *7* (1), 18054.
12. Dai, C.; Li, Y.; Pan, W.; Wang, G.; Huang, R.; Bu, Y.; Liao, X.; Guo, K.; Gao, F., Three-Dimensional High-Porosity Chitosan/Honeycomb Porous Carbon/Hydroxyapatite Scaffold with Enhanced Osteoinductivity for Bone Regeneration. *ACS Biomater Sci Eng* **2020,** *6* (1), 575-586.
13. Jana, S.; Florczyk, S. J.; Leung, M.; Zhang, M., High-strength pristine porous chitosan scaffolds for tissue engineering. *Journal of Materials Chemistry* **2012,** *22* (13).
14. Huang, L.; Xiao, L.; Jung Poudel, A.; Li, J.; Zhou, P.; Gauthier, M.; Liu, H.; Wu, Z.; Yang, G., Porous chitosan microspheres as microcarriers for 3D cell culture. *Carbohydr Polym* **2018,** *202*, 611-620.
15. Qian, L.; Zhang, H., Controlled freezing and freeze drying: a versatile route for porous and micro-/nano-structured materials. *Journal of Chemical Technology & Biotechnology* **2011,** *86* (2), 172-184.

16. Ren, L.; Xu, J.; Zhang, Y.; Zhou, J.; Chen, D.; Chang, Z., Preparation and characterization of porous chitosan microspheres and adsorption performance for hexavalent chromium. *Int J Biol Macromol* **2019,** *135*, 898-906.
17. Maleki, H.; Duraes, L.; Garcia-Gonzalez, C. A.; Del Gaudio, P.; Portugal, A.; Mahmoudi, M., Synthesis and biomedical applications of aerogels: Possibilities and challenges. *Adv Colloid Interface Sci* **2016,** *236*, 1-27.
18. Pandis, C.; Madeira, S.; Matos, J.; Kyritsis, A.; Mano, J. F.; Ribelles, J. L., Chitosan-silica hybrid porous membranes. *Mater Sci Eng C Mater Biol Appl* **2014,** *42*, 553-61.
19. Li, J.; Wu, X.; Wu, Y.; Tang, Z.; Sun, X.; Pan, M.; Chen, Y.; Li, J.; Xiao, R.; Wang, Z.; Liu, H., Porous chitosan microspheres for application as quick in vitro and in vivo hemostat. *Mater Sci Eng C Mater Biol Appl* **2017,** *77*, 411-419.
20. Bharadwaz, A.; Jayasuriya, A. C., Fabrication of porous chitosan particles using a novel two-step porogen leaching and lyophilization method with the label-free multivariate spectral assessment of live adhered cells. *Colloids Surf B Biointerfaces* **2021,** *208*, 112094.
21. Liu, Y.; Cai, Z.; Jin, Y.; Sheng, L.; Ma, M., Volcanic Rock-Inspired Fabrication of Porous Chitosan Macroparticles via Gas Porogen for Enhancing the Activity of Immobilized Enzymes. *ACS Sustainable Chemistry & Engineering* **2020,** *8* (41), 15560-15572.
22. Xu, J. H.; Zhao, H.; Lan, W. J.; Luo, G. S., A novel microfluidic approach for monodispersed chitosan microspheres with controllable structures. *Adv Healthc Mater* **2012,** *1* (1), 106-11.
23. Yang, Y.; Chen, G.; Murray, P.; Zhang, H., Porous chitosan by crosslinking with tricarboxylic acid and tuneable release. *SN Applied Sciences* **2020,** *2* (3).
24. Mahaninia, M. H.; Wilson, L. D., Cross-linked chitosan beads for phosphate removal from aqueous solution. *Journal of Applied Polymer Science* **2016,** *133* (5), n/a-n/a.
25. Giraldo, S.; Robles, I.; Godinez, L. A.; Acelas, N.; Florez, E., Experimental and Theoretical Insights on Methylene Blue Removal from Wastewater Using an Adsorbent Obtained from the Residues of the Orange Industry. *Molecules* **2021,** *26* (15).
26. Oladoye, P. O.; Ajiboye, T. O.; Omotola, E. O.; Oyewola, O. J., Methylene blue dye: Toxicity and potential elimination technology from wastewater. *Results in Engineering* **2022,** *16*.
27. Liu, W.; Zhang, Y.; Wang, S.; Bai, L.; Deng, Y.; Tao, J., Effect of Pore Size Distribution and Amination on Adsorption Capacities of Polymeric Adsorbents. *Molecules* **2021,** *26* (17).
28. Fernandes Queiroz, M.; Melo, K. R.; Sabry, D. A.; Sassaki, G. L.; Rocha, H. A., Does the use of chitosan contribute to oxalate kidney stone formation? *Mar Drugs* **2014,** *13* (1), 141-58.
29. Zeng, L.; Qin, C.; Wang, L.; Li, W., Volatile compounds formed from the pyrolysis of chitosan. *Carbohydrate Polymers* **2011,** *83* (4), 1553-1557.
30. Debritto, D.; Campana-Filho, S. P. A., A kinetic study on the thermal degradation of N,N,N-trimethylchitosan. *Polymer Degradation and Stability* **2004,** *84* (2), 353-361.
31. Wong, Y. C.; Szeto, Y. S.; Cheung, W. H.; McKay, G., Adsorption of acid dyes on chitosan—equilibrium isotherm analyses. *Process Biochemistry* **2004,** *39* (6), 695-704.
32. Wang, L. G.; Li, Z.; Zhang, L.; Zhou, R.; Chen, X., On the Measurement of Particle Contact Curvature and Young's Modulus Using X-ray µCT. *Applied Sciences* **2021,** *11* (4).
33. Silva, N. V.; Angulo, S. C.; da Silva Ramos Barboza, A.; Lange, D. A.; Tavares, L. M., Improved method to measure the strength and elastic modulus of single aggregate particles. *Materials and Structures* **2019,** *52* (4).

34. Russell, A.; Schmelzer, J.; Müller, P.; Krüger, M.; Tomas, J., Mechanical properties and failure probability of compact agglomerates. *Powder Technology* **2015,** *286*, 546-556.

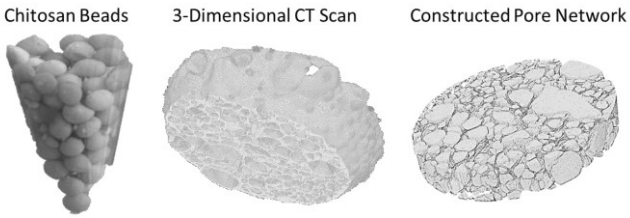

Synopsis: Three-dimensional (3D) computed tomography (CT) scanning was used to visualize and measure the porosity of different particle types